nature communications

Article

https://doi.org/10.1038/s41467-025-61705-1

Magnetic signatures and origins of ferromagnetic minerals in Chang'e-6 lunar farside soils

Received: 15 April 2025

Accepted: 26 June 2025

Published online: 05 July 2025

Check for updates

Jinhua Li[1,2] ✉, Lin Xing[1,2], Zheng Gong[3], Jiawei Liu[2,4], Yan Liu[1,2], Weiwei Wu[1,2], Kelei Zhu[1,2], Yuqin Wang[1,2], Xu Tang[1,2], Lixin Gu[1,2], Yi Chen[2,5], Qiuli Li[2,5], Zhaoyang Cao[1,2], Shuangchi Liu[2,5], Shuhui Cai[2,5] & Yongxin Pan[2,4]

Ferromagnetic minerals in lunar materials record key information regarding the Moon's ancient dynamo, impact events, and space weathering. However, interpreting the magnetic signals is complicated by their diverse origins and properties. Here, we present comprehensive magnetic and mineralogical results of farside lunar soils returned by Chang'e-6 mission from the South Pole-Aitken Basin. Compared to nearside samples, these soils exhibit higher magnetic susceptibility and saturation magnetization, and the highest saturation remanence, despite weak local crustal magnetic anomalies. Advanced electron microscopy reveals two primary mineralogical populations: nickel-poor iron particles with euhedral shapes in basalt clasts (magmatic origin) and nickel-rich metallic iron and Fe-Ni alloys in breccias, agglutinates, and glassy materials (impact origin). These findings offer insights into the formation of magnetic minerals on the lunar farside, thereby enhancing our understanding of lunar dynamo evolution and crustal magnetic anomalies.

Understanding the magnetism of lunar materials is fundamental to deciphering the Moon's geological history, as ferromagnetic minerals in lunar materials preserve valuable information regarding the evolution of the Moon's ancient internal dynamo and surface processes, such as meteorite impacts and space weathering[1–4]. Studies using lunar samples and orbital magnetic field measurements show that the Moon retains a present-day remanent crustal magnetization, indicative of an ancient lunar dynamo[5]. However, due to the limited availability of samples and geophysical data, the temporal evolution and sustaining mechanism of the lunar dynamo, as well as the origins of crustal magnetic anomalies, remain uncertain[3,6–10].

The lunar surface environment is characterized by its airless, anhydrous, and strongly reducing conditions[11,12]. Therefore, unlike the magnetic oxides and sulfides that are commonly in terrestrial environments, the primary carriers of magnetic remanence are metallic iron and Fe-Ni alloys, including kamacite (α-$Fe_{1-\chi}Ni_\chi$ with $\chi \le 0.05$), taenite (α_2-$Fe_{1-\chi}Ni_\chi$ with $\sim 0.05 \le \chi \le 0.25$), and iron phosphide schreibersite ($[Fe_{1-\chi}Ni_\chi]_3P$ with $\chi \sim 0.1$)[1,13,14]. These minerals originate from both endogenous magmatic processes and exogenous meteoritic inputs, exhibiting considerable variations in grain size, morphology, nickel content, crystallographic structure, and internal stress state[5,13,15–17]. This variability fundamentally influences magnetic remanence acquisition and stability mechanisms and their stabilities, yet atomic-scale characterization remains limited. Proposed sources for remanence acquisition include dynamo-driven magnetic fields[3,6,7,18], transient impact-generated fields[9,19,20], and plasma-induced field amplification[21,22].

[1]Key Laboratory of Deep Petroleum Intelligent Exploration and Development, Institute of Geology and Geophysics, Chinese Academy of Sciences, Beijing 100029, China. [2]College of Earth and Planetary Sciences, University of Chinese Academy of Sciences, Beijing 100049, China. [3]State Key Laboratory for Critical Earth Material Cycling and Mineral Deposits, School of Earth Sciences and Engineering, Nanjing University, Nanjing 210023, China. [4]Key Laboratory of Earth and Planetary Physics, Institute of Geology and Geophysics, Institute of Geology and Geophysics, Chinese Academy of Sciences, Beijing 100029, China. [5]State Key Laboratory of Lithospheric and Environmental Coevolution, Institute of Geology and Geophysics, Chinese Academy of Sciences, Beijing 100029, China. ✉e-mail: lijinhua@mail.iggcas.ac.cn

South Pole-Aitken (SPA) Basin (~ 4.25 Ga), the Moon's largest and deepest impact structure[23–27], displays pronounced crustal magnetic anomalies along its northern rim but relatively weak crustal magnetization in the central region[28,29] (Fig. 1b). Numerical modeling indicates that CE6 samples originate from areas affected by impact melts during Apollo (~ 4.14–3.91 Ga) and SPA Basin formation events[26,30], combined with lithic fragments of diverse ejecta[26,31–33]. Recent Pb-Pb dating identified two basaltic volcanism episodes (~ 4.2 Ga and ~2.8 Ga)[34,35]. Non-heating paleomagnetic analyses based on ARM (anhysteretic remanent magnetization) and IRM (isothermal remanent magnetization) suggest relatively strong field intensities (5–21 μT) during the second volcanic phase[7], although the accurate paleointensities have yet to be confirmed by thermal studies, such as Thellier-series experiments.

In this study, we present comprehensive magnetic and atomic-scale mineralogical analyses of lunar soils returned by the Chang'e-6 (CE6) mission from the SPA Basin, near the southern rim of the Apollo crater[31,32] (Fig. 1a, Supplementary Fig. 1). We provide comprehensive magnetic-mineralogical characterization of lunar farside soils, offering insights into lunar dynamo evolution, mechanisms underlying crustal magnetization, and the role of impact processes in generating magnetic anomalies. This study contributes to the understanding of the Moon's complex geological history and future lunar explorations.

Results

Bulk magnetic properties of CE6 soils

Bulk magnetic properties of the CE6 soil sample (CE6_S1, ~149.8 mg) measured at room conditions are summarized in Supplementary Data 1. The hysteresis loop displays a slightly wasp-waisted shape (Fig. 1c), with coercivity (B_c) of 3.88 mT and remanence coercivity (B_{cr}) of 33.77 mT, indicating a mixture of low-coercivity magnetic components of varying grain sizes or compositions, or both[36]. Frequency-dependent susceptibility (χ_{fd}%) is ~8.8%, suggesting the presence of abundant ultrafine superparamagnetic (SP) grains[37]. A first-order reversal curves (FORC) diagram exhibits a "butterfly-like" pattern with a narrow, high-coercivity tail (~ 60–100 mT) (Fig. 1d), indicative of single-vortex (SV) and minor single-domain (SD) grains as principal carriers of magnetic remanence[38].

Unmixing of IRM curves reveals three coercivity components (Fig. 1e): a low-coercivity component ($B_{1/2}$ = 4.0 mT, ~10.4% IRM), mid-coercivity component ($B_{1/2}$ = 19.1 mT, ~42.3% IRM), and high-coercivity component ($B_{1/2}$ = 93.3 mT, ~47.3% IRM). Compared to the soils

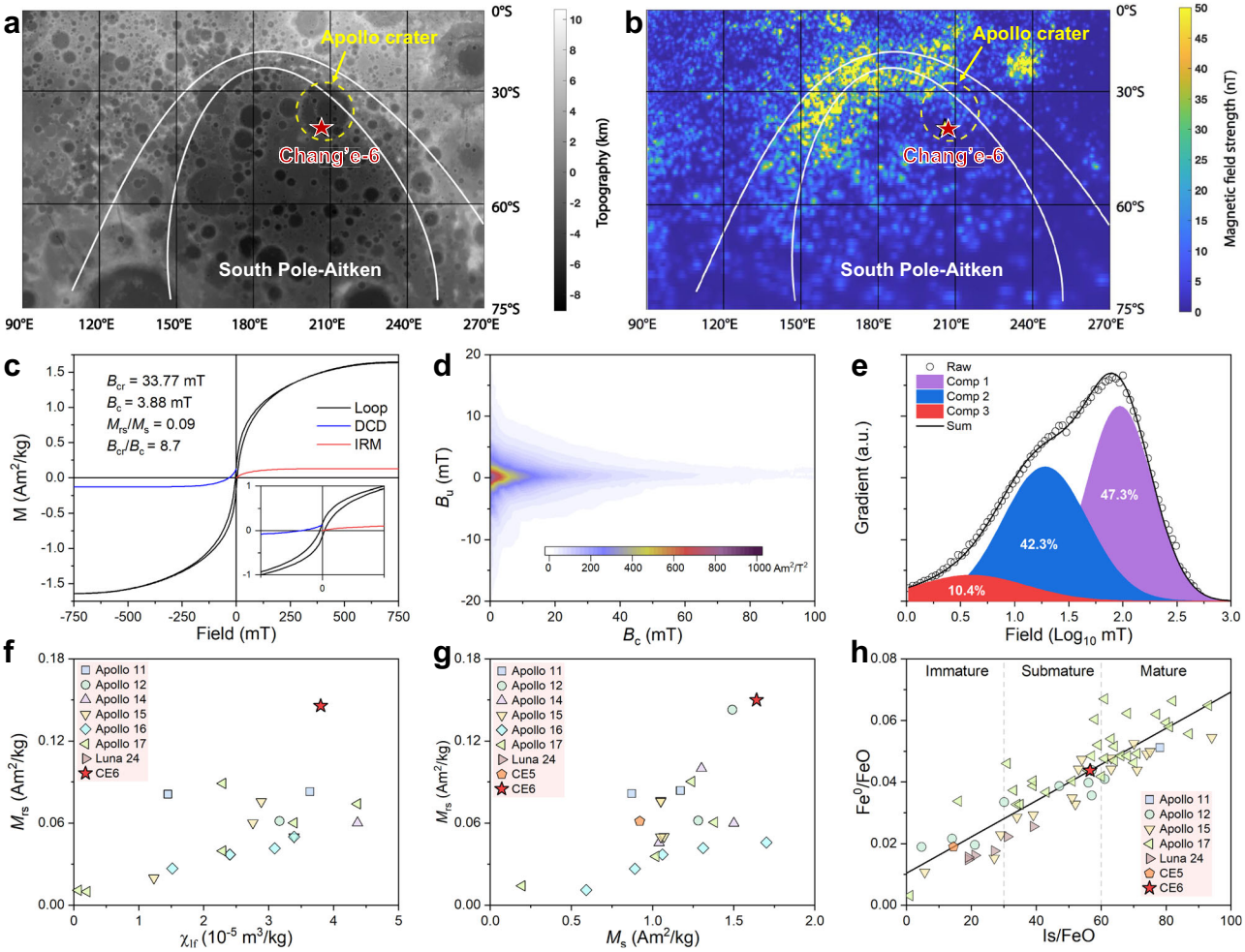

Fig. 1 | Magnetic properties of the CE6 lunar soils. a Topographic map showing the CE6 landing site within the South Pole-Aitken (SPA) Basin. White ellipses (partial view) oriented north-south indicate best-fit inner and outer structural rims of the SPA Basin (modified from ref. 23). **b** Map illustrating the lunar crustal magnetic field strengths projected on the lunar surface near the CE6 landing region (data from ref. 29). **c**–**e** Representative magnetic measurements of CE6 soils: (**c**) magnetic hysteresis loop (black), and corresponding isothermal remanence magnetization (IRM, red) acquisition and direct current demagnetization (blue) curves; (**d**) first-order reversal curves (FORC) diagram illustrating magnetic domain states and interactions; and (**e**) decomposition of IRM acquisition curve revealing three coercivity components. **f**, **g** Scatter plots comparing low-frequency magnetic susceptibility (χ_{lf}) versus saturation remanence (M_{rs}) (**f**, data from ref. 13), and M_{rs} versus saturation magnetization (M_s) (**g**, data from ref. 33), placing CE6 soils in context with nearside lunar soils from Apollo, Luna, and Chang'e-5 missions. **h** Plot of the Fe^0/FeO versus Is/FeO (ferromagnetic resonance intensity normalized by total iron content, data from ref. 33), showing the high maturity level of CE6 soils.

https://doi.org/10.1038/s41467-025-61705-1

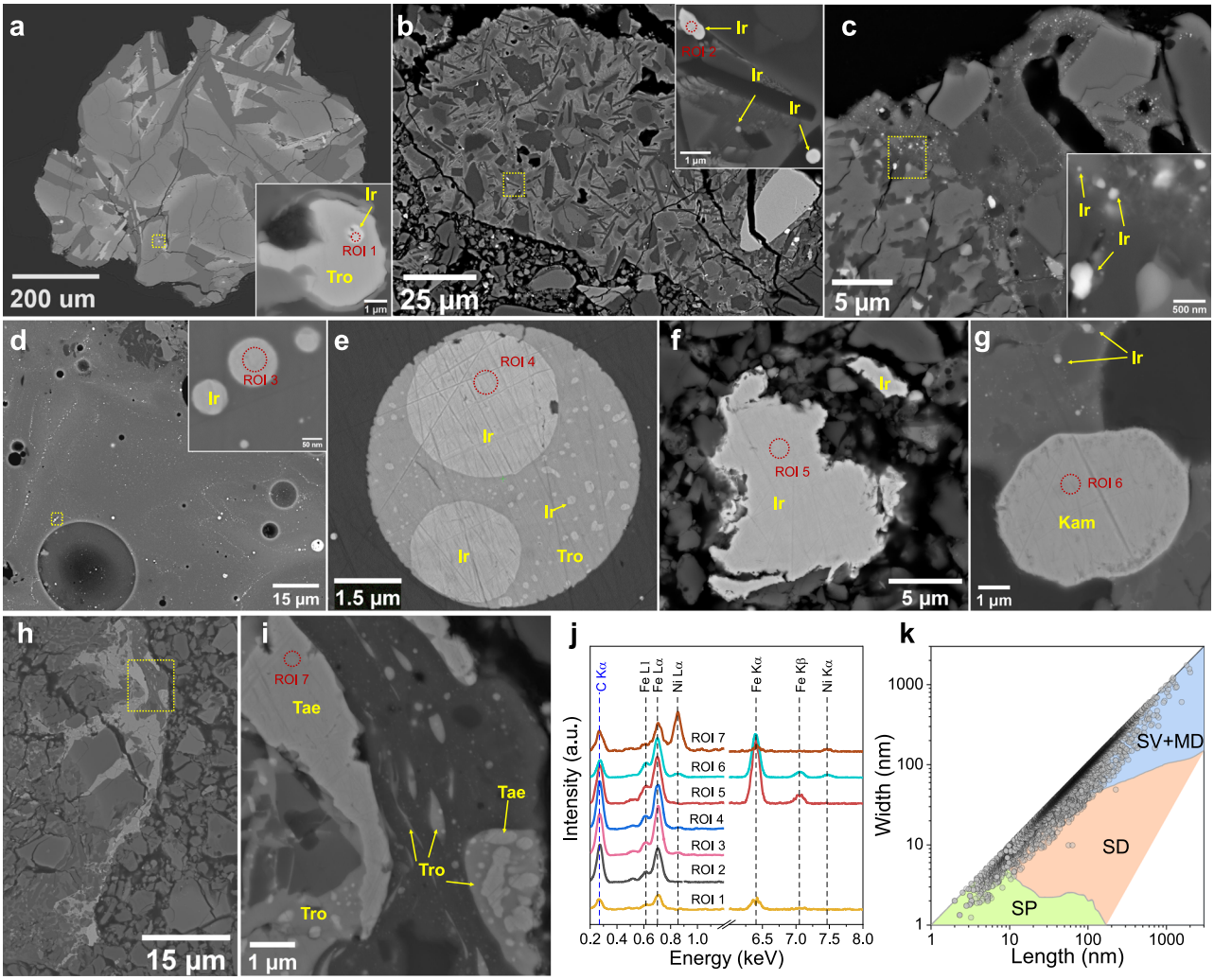

Fig. 2 | BSE-SEM characterization of ferromagnetic minerals in CE6 soils. a-d Representative backscattered electron scanning electron microscopy (BSE-SEM) images of ferromagnetic minerals in basaltic clast **(a)**; basaltic impact melt **(b)**; agglutinate **(c)**; and glassy agglutinate **(d)**. Insets show magnified details from regions indicated by the dashed yellow boxes. **e** Glassy agglutinate with abundant spherical and irregular metallic iron (Ir) grains associated with troilite (Tro). **f, g** Micron-sized metallic iron particles **(f)** and Fe-Ni alloy (kamacite, Kam) crystals **(g)** within agglutinates. **h** Troilite veins associated with taenite (Tae) assemblages in an agglutinate particle. **i** Enlarged detail of panel **h** showing troilite-taenite intergrowth. **j** SEM-based energy dispersive X-ray spectroscopy (SEM-EDXS) spectra from regions (dashed red circles in panels **a-g** and **i**) confirming compositions of metallic iron or Fe-Ni alloys. **k** Grain-size distribution of metallic iron particles in CE6 soils, indicating their potential superparamagnetic (SP), single-domain (SD), single-vortex (SV), or multidomain (MD) behaviors (boundaries adapted from ref. 41). Basaltic materials contain rare, nickel-poor iron grains, whereas agglutinates and glassy materials have abundant iron particles with elevated, variable nickel contents. Additional high-resolution SEM images and SEM-EDXS compositional maps are provided in supplementary Figs. 4–13.

returned by Apollo, Luna, and Chang'e-5 (CE5) missions (Supplementary Data 2), the CE6_S1 sample exhibits notably higher low-frequency magnetic susceptibility (χ_{lf}), saturation magnetization (M_s), and the highest saturation remanence (M_{rs} = 0.15 Am^3/kg) (Fig. 1f, g). These results are consistent with the high abundance of ferromagnetic minerals within the CE6 soils, capable of carrying strong magnetic remanence.

Furthermore, CE6 soils exhibit significantly higher M_{rs} and M_s values relative to lunar basaltic rocks (Supplementary Fig. 2). Using the empirical linear relationship between Fe /FeO and Is/FeO[39], we estimate metallic iron content in CE6_S1 at ~0.75%, corresponding to an Is/FeO ratio of 56.5 (Fig. 1h). These values are comparable to the typical values of mature lunar soils[33,40], pointing toward extensive space weathering at the landing site.

Ferromagnetic minerals in CE6 soils

Three-dimensional X-ray microscopy (3D-XRM) shows CE6 soils composed of diverse basalt, breccia, agglutinate, and glass clasts (Supplementary Fig. 3, Supplementary Movie 1), consistent with previous scanning electron microscopy (SEM) observations[32]. SEM imaging combined with backscattered electron (BSE) and energy dispersive X-ray spectroscopy (EDXS) mapping indicates rare, submicron-sized iron particles sparsely distributed in basalt clasts, frequently associated with troilite (Fig. 2a, and Supplementary Figs. 4–5).

In contrast, agglutinates, glasses, and glassy agglutinates host abundant metallic iron particles predominantly nanometer to submicron in size (Fig. 2b–e, and Supplementary Fig. 6). Iron particles in glassy materials commonly show spherical shapes, whereas those in basaltic impact melts and non-glassy agglutinates are generally euhedral or irregular (Fig. 2b–d). Additionally, micron-sized troilite spheres containing dense metallic iron aggregations are occasionally observed in glassy agglutinates (Fig. 2e). Iron-rich metallic particles and veins are also sporadically present in agglutinates and breccia (Fig. 2f–i).

EDXS analyses reveal nickel-poor metallic iron particles within basaltic materials (Fig. 2j, and Supplementary Figs. 5–7), indicating a

magmatic origin. Conversely, iron particles in agglutinates and glasses exhibit variable nickel contents, generally below 5% Ni/(Fe+Ni) (Supplementary Figs. 8–9). Occasionally, larger metallic grains identified include pure metallic iron (Supplementary Fig. 10) or Fe-Ni alloy kamacite (Ni ~5–10%, Supplementary Figs. 11–12). Fe-rich veins observed in breccias predominantly consist of troilite or mixtures of troilite and Ni-rich taenite, exhibiting Ni/(Fe+Ni) ratios over 20% (Supplementary Fig. 13).

Given their abundant occurrences and nano- to submicron- sizes (Fig. 2k), the metallic iron grains likely show diverse magnetic behaviors, including SP, SD, SV, and possibly multidomain (MD) states[41].

Ultrastructural and mineralogical characterization of ferromagnetic minerals in CE6 soils

The heterogeneous distribution of ferromagnetic minerals in basaltic and non-basaltic components of CE6 soils suggests distinct formation pathways. To better constrain these processes, representative samples, including basalt (FIB_1), basaltic impact melt (FIB_2), glassy agglutinate (FIB_3), kamacite microcrystal (FIB_4), and a troilite-taenite vein (FIB_5), were investigated at atomic scales using transmission electron microscopy (TEM) on ultrathin sections prepared via focused ion beam (FIB) milling (Supplementary Fig. 14).

TEM analyses revealed clear morphological and compositional differences among the ferromagnetic particles. Iron grains within basaltic materials predominantly exhibit euhedral shapes and were consistently nickel-poor (Supplementary Figs. 15, 16), suggesting endogenous crystallization processes, likely associated with fractional crystallization within lunar basaltic lava flows or the lunar magma ocean[15,42].

In contrast, iron particles within glassy agglutinates are predominantly spherical or ellipsoidal, with significant nickel enrichment and notable compositional variability among individual particles, and even within single grains (Supplementary Fig. 17). The prevalence of these nickel-rich Fe-Ni alloys and their spherical morphology indicates substantial exogenous contributions, likely originating from iron-rich or chondritic meteorite influx[26,32,43]. Repeated impact events facilitated the rapid cooling of impact-generated melts, forming abundant spherical iron particles at nano- to micron-scales[14,44,45]. Diffusion of meteoritic nickel into pre-existing metallic iron during these repeated impact events can explain the observed compositional diversity of Fe-Ni alloys in non-basaltic materials[46].

Additionally, TEM analyses revealed the unexpected occurrence of detectable phosphate within the kamacite microcrystals (Supplementary Fig. 18a–d), unveiling previously unrecognized compositional complexities in lunar metallic minerals. Notably, numerous metallic Fe and Fe-Ni alloy particles exhibit close spatial relationships with troilite (Supplementary Figs. 18–21). In particular, pentlandite intergrowths bridging troilite and taenite phases were clearly identified (Fig. 3, and Supplementary Figs 19, 20), supporting an exsolution origin for certain Fe-Ni alloy particles from sulfide precursors.

High-resolution TEM and selected-area diffraction pattern (SAED) further confirms that the metallic iron particles possess kamacite-type (α-Fe) structures characterized by a body-centered cubic (BCC) lattice (Supplementary Figs. 15, 16, 18). These ultrastructural observations provide critical insights into the complex and diverse formation pathways of ferromagnetic minerals at the CE6 landing site.

Discussion

The SPA soils represent a complex, time-integrated assemblage that preserves a unique record of lunar surface and subsurface processes over more than four billion years[27,32,47,48]. These soils encapsulate: (i) the basin's formation through a massive impact event at ~4.25 Ga, followed by sustained bombardments during the Late Heavy Bombardment period (~4.2–3.9 Ga); (ii) episodes of farside mare volcanism between ~4.2 and 2.8 Ga, driven by mantle-derived magmatism through the regions anomalously thin crust; (iii) ~3.9 billion years of continuous micrometeoroid bombardment and solar wind irradiation, resulting in progressive space weathering of soil particles; and (iv) late state regolith reworking and cryogenic modification within the last 1 billion years, primarily due to small-scale impacts and polar thermal cycling.

Our detailed microscopic analyses reveal a heterogeneous distribution and diverse formation pathways of ferromagnetic minerals within the CE6 soils, closely related to the complex geological context and history of the SPA Basin. First, the rare, euhedral-to-irregular, nickel-poor metallic iron grains found in basaltic materials likely crystallized endogenously, either through fractional crystallization of lunar magma or surface cooling of basaltic lava flows. These particles probably formed via exsolution from iron-bearing silicates (e.g., pyroxene, olivine) or sulfide minerals such as troilite[42,46]. Second, some iron particles and Fe-Ni alloys in breccias and basaltic impact melts could have been transported from distant volcanic sources, followed by recrystallization induced by subsequent impacts[32,49,50]. Third, significant exogenic contributions, reflected by nickel-rich metallic iron and Fe-Ni alloy particles abundant in agglutinates and glassy materials, suggest meteoritic influx, likely involving chondritic or iron-rich meteorites[26,32,43]. Fourth, repeated impacts at the SPA Basin promoted rapid cooling of melt droplets, forming abundant nano- to micron-scale spherical metallic iron grains enriched in nickel from meteoritic sources[14,27,44,46]. Moreover, additional lunar surface processes lead to additional complexities in the ferromagnetic mineralogy of the CE6 soils. For instance, solar wind irradiation produces nanophase iron embedded within lunar soil grain rims[51–53]. Similarly, impact events and galactic cosmic irradiation (GCR) can vaporize surface materials and subsequently deposit metallic iron or Fe-Ni alloy onto existing regolith grains[45,54].

Both our bulk magnetic measurements and microscopic observations reveal diverse grain-size distributions and magnetic domain states of these metallic Fe particles within CE6 soils. SP grains are indicated by significant frequency-dependent susceptibility, while SD and SV populations are suggested by the FORC diagrams. Larger grains, consistent with MD behavior, are evident microscopically (Fig. 2k). This diversity allows the lunar soils to record multiple forms of remanent magnetizations (Fig. 4). Primary basaltic clasts acquire thermoremanent magnetization (TRM) as they cool through their unblocking temperatures. Space-weathered grains record chemical remanent magnetization (CRM), while hypervelocity impacts impart shock remanent magnetization (SRM). During settling through the exosphere, random reorientation of individual TRMs yields a net depositional-style remanent magnetization (DRM), despite the Moon's anhydrous environment. Finally, prolonged exposure to weak lunar ambient fields can impart viscous remanent magnetization (VRM), as low-coercivity grains gradually acquire small, time-dependent moments that may partially overprint older signals.

The long-term stability of remanent magnetization depends on the magnetic carriers' intrinsic properties, the strength and geometry of the ambient field at acquisition, and any subsequent alteration or shock overprinting. Compared to magnetite, SD to SV metallic iron and Fe-Ni alloys (including kamacite and Ni-rich Fe phases) benefit from much higher Curie temperatures[55,56], enhancing their thermal unblocking thresholds. However, relative to SD-SV magnetite, their higher saturation magnetization and lower intrinsic coercivities[16,55,57], render them more susceptible to shock-induced domain wall pinning and to surface defects generated by space weathering. Although some Fe-Ni grains may acquire thermochemical remanent magnetization (TCRM) during post-formation crystal growth[5], recent micromagnetic models and laboratory experiments show that nanometer-scale taenite can retain stable primary magnetization over geological timescales, thanks to coercivities approaching ~250 mT[58,59].

https://doi.org/10.1038/s41467-025-61705-1

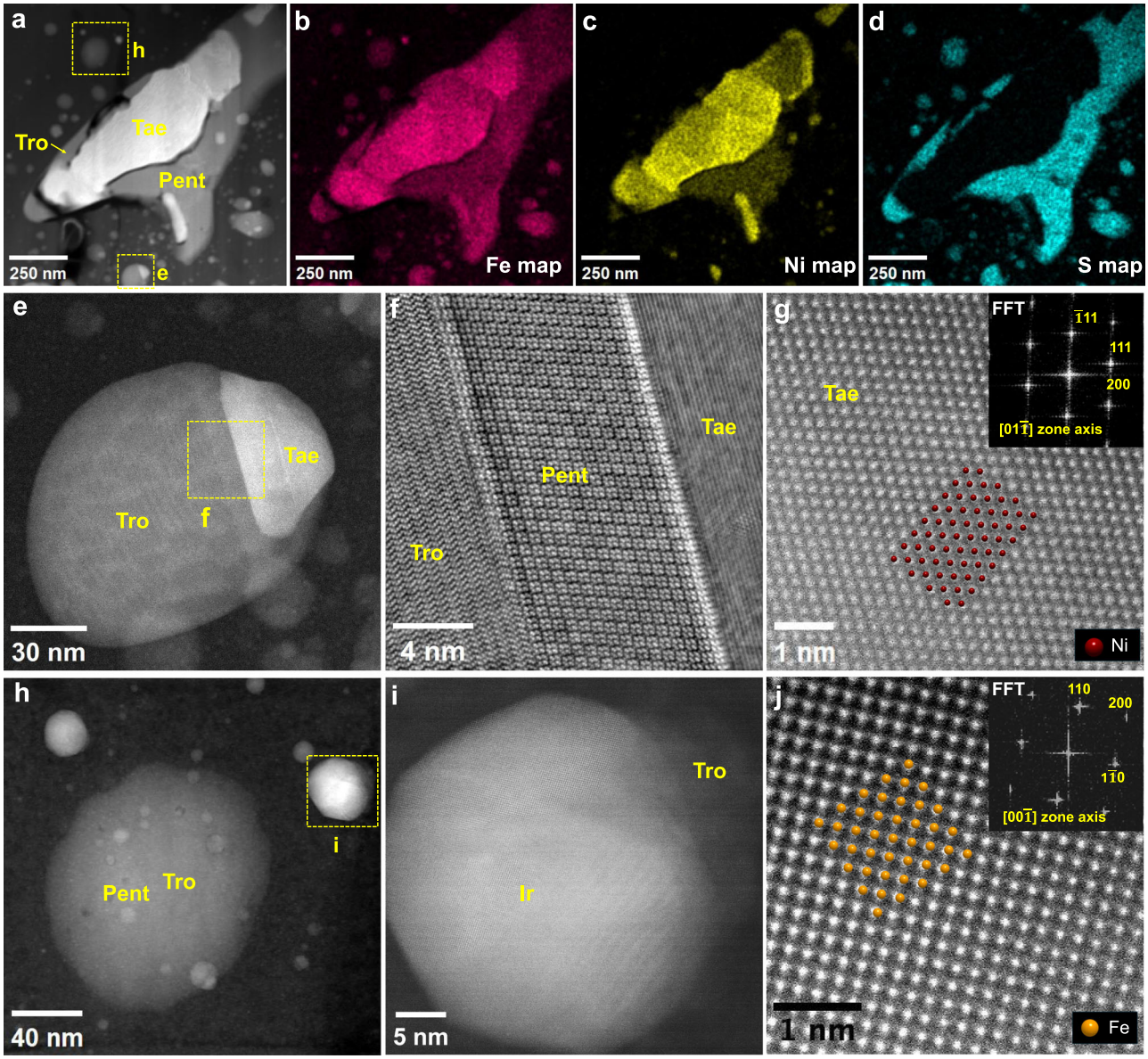

Fig. 3 | TEM characterization of ferromagnetic minerals in a troilite-taenite vein (sample FIB_5). a High-angle annular dark-field scanning transmission electron microscopy (HAADF-STEM) image illustrating morphological and size variations among troilite (Tro), pentlandite (Pent), and taenite (Tae). **b**–**d** STEM-EDXS elemental maps of Fe (Fe Kα, **b**), Ni (Ni Kα, **c**), and S (S Kα, **d**), revealing compositional heterogeneity. **e** Magnified HAADF-STEM image (area marked in lower dashed yellow box in **a**) detailing troilite-pentlandite-taenite interfaces. **f** Atomic-resolution HAADF-STEM image of troilite-pentlandite-taenite interfaces viewed along troilite [$\bar{1}$100] and pentlandite [01$\bar{1}$] crystallographic axes. **g** Atomic-resolution HAADF-STEM image of taenite (area in **e**) viewed along [01$\bar{1}$]; inset shows the corresponding fast Fourier transform (FFT) diffraction pattern and atomic structure model (iron atoms not invisible along this orientation). **h** Magnified HAADF-STEM image (upper dashed yellow box in **a**) of troilite-metallic iron assemblage, adjacent to troilite with pentlandite **i**nclusions. **i** Atomic-resolution HAADF-STEM image of troilite-metallic iron interface highlighted in (**h**). **j** Atomic-resolution HAADF-STEM image of metallic **i**ron in panel **i**. The inset (upper right) shows an FFT diffraction pattern, with a superimposed theoretical atomic model confirming the α-iron (body-centered cubic, BCC) crystal structure. Additional TEM characterizations of other FIB samples are provided in supplementary Figs. 15–18; detailed STEM-EDXS data in supplementary Figs. 19–21.

The complex assemblage of ferromagnetic minerals and their distinct magnetization acquisition mechanisms place important constraints on lunar magnetic field evolution, crustal magnetic anomalies, and space weathering processes. For instance, although CE6 soils exhibit remarkably high remanence-carrying capacity (high M_{rs} values), the landing region shows relatively weak crustal magnetic anomalies (Fig. 1). This paradox likely results from repeated thermal demagnetization associated with impacts occurring after the lunar dynamo significantly weakened or ceased. Conversely, the pronounced crustal magnetic anomaly in the northwestern margin of the SPA Basin likely results from accumulated ejecta composed of meteoritic and impact-generated metallic iron, consistent with prior modeling results[28]. Based on the modeling of ref. 28, materials with low thermal susceptibility must form much thicker layers than those with high susceptibility to reproduce the SPA magnetic anomaly. Exogenous components, such as meteoritic and impact-generated metallic iron are characterized by high thermal susceptibility, and thus are the most efficient contributors to the SPA signal. Although our M_{rs} measurement represents a bulk soil property, it is the highest reported among returned lunar samples, implying a disproportionately large abundance of metallic Fe and Fe–Ni alloys in the Chang'e-6 soils, as confirmed by electron microscopic analyses. This enrichment of

https://doi.org/10.1038/s41467-025-61705-1

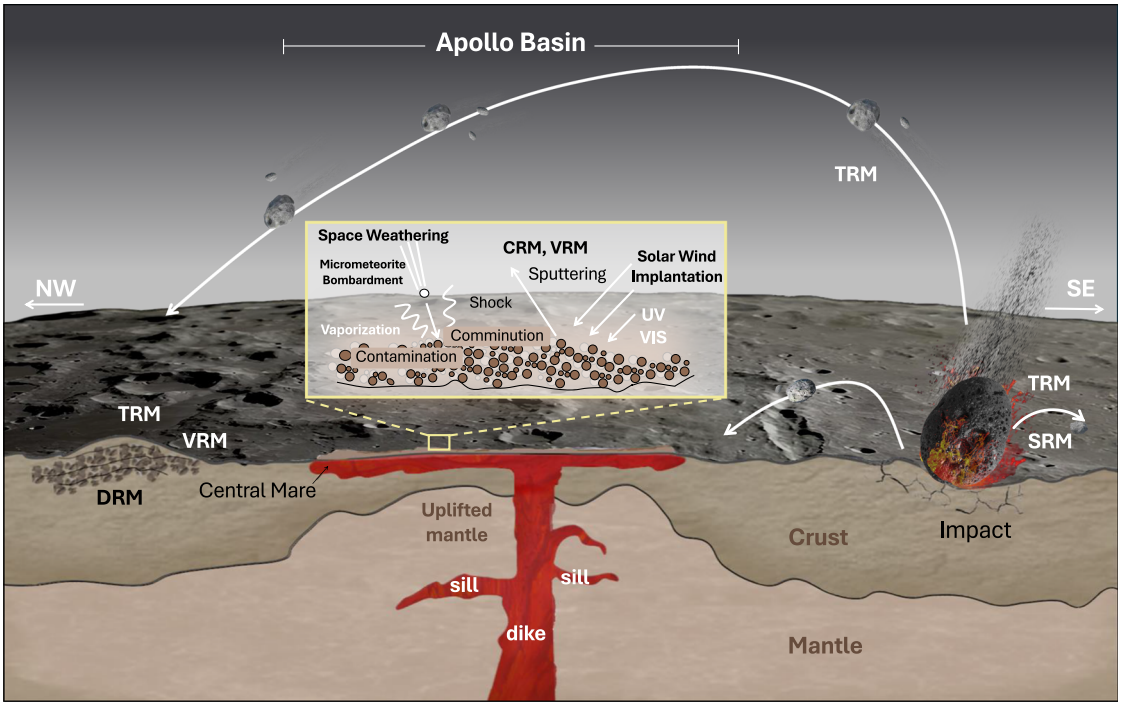

Fig. 4 | Schematic summary illustrating formation pathways of ferromagnetic minerals in CE6 lunar soils and their corresponding remanent magnetization acquisition mechanisms. Formation pathways include fractional crystallization from lunar magma and cooling of basaltic lava flows; recrystallization via impact-induced melting, delivery and deposition of exogenous meteoritic iron-rich materials; formation of spherical nano- to micron-scale metallic iron grains through impacts; and space-weathering processes such as solar wind irradiation and vapor deposition. These diverse origins make ferromagnetic minerals exhibit distinct physical, chemical, and magnetic properties, enabling the acquisition of various remanent magnetization: thermal (TRM), chemical (CRM), shock (SRM), viscous (VRM), and depositional (DRM). The coexistence of these magnetizations in lunar materials provides essential constraints for interpreting lunar dynamo history, crustal magnetic anomalies, and surface weathering evolution. The SPA crustal-structure model is adopted from refs. 50,73., while our framework for space-weathering processes follows ref. 14. The topographic map of the moon is modified from ref. 74. (NASA\SVS\Ernest T. Wright).

high–thermal-susceptibility phases substantially reduces the minimum volume of material required to account for the SPA anomaly.

Numerous paleointensity studies conducted on whole-rock lunar samples returned by Apollo and Chang'e missions, as well as lunar meteorites, support the existence of an internally generated lunar magnetic field active approximately between 4.2 and 1.5 Ga[1,3,6–8,17,18,60]. In contrast, recent single-crystal paleointensity analyses of the Apollo samples cast doubt on this long-lived lunar dynamo hypothesis[9,10,61], indicating that previously reported high paleointensity values might reflect secondary magnetizations induced by shock or impact-related processes[9]. These discrepancies regarding the age of the lunar dynamo partly stem from methodological challenges. For example, Thellier-type experiments, which rely on repeated and prolonged laboratory heating, can modify the microstructure and composition of lunar Fe-Ni alloys and metallic iron, thereby compromising the fidelity of the recorded field[62,63]. To avoid heating artifacts, alternating-field methods (e.g., ARM, IRM) apply empirical calibration factors (f, a) derived from single-mineral standards to the heterogeneous mixture of ferromagnetic phases in lunar soils[64]. This practice can introduce uncertainties of a factor of ~2–5 relative to true ancient field strengths[5,65,66].

Addressing these limitations demands a systematic, high-resolution characterization of magnetic carriers in the lunar materials. Advanced analytical methods, including atomic-scale SEM and TEM analyses, can differentiate magnetic mineral populations based on their formation processes. Specifically, certain magnetic minerals, such as euhedral, nickel-poor metallic iron grains in lunar basalts, may reliably record primary lunar dynamo signals. Additionally, emerging magnetic microscopy techniques promise to deliver paleointensity determinations with unprecedented spatial resolution[67]. Targeted investigations of impact-generated further enable the separation of primary lunar dynamo signals from secondary shock-induced remanences[5,6,9,18,68]. Ultimately, integrating these advanced analytical methods with improved paleointensity protocols will be essential to unravel the complex history of the Moon's magnetic field and its geophysical implications.

Methods

Sample preparation

The CE6 lunar samples analyzed in this study include two aliquots of surface scooped soils (CE6C0200YJFM001 and CE6C0100YJFM002) allocated by the China National Space Administration. ~149.8 mg of soil was loaded into a non-magnetic gelatin capsule for bulk magnetic analyses and non-destructive 3D XRM imaging. Individual basaltic and breccia grains were manually selected under an optical microscope, embedded in epoxy resin mounts, mechanically polished following standard grinding procedures, and carbon-coated for electron microscopy. All rock magnetic and microscopic experiments were performed at the Palemagnetism and Geochronology Laboratory (PGL) and Electron Microscopy Laboratory (EML), Institute of Geology and Geophysics, Chinese Academy of Sciences, Beijing.

Rock magnetic measurements

Mass-specific magnetic susceptibility was measured at low frequency (χ_{lf} = 967 Hz) and high frequency (χ_{hf} = 15,616 Hz) using an Agico Multifunction Kappabridge susceptibility meter (model MFK2-FA), with an applied field strength of 200 A/m. To minimize measurement uncertainty, each sample was measured five times, and the average susceptibility values were used.

Magnetic hysteresis loops, direct current (DC) demagnetization curves, IRM, and FORCs were measured using a Princeton MicroMag 3900 vibrating sample magnetometer (VSM; sensitivity = 5.0×10^{-9} Am²). Hysteresis loops were acquired in discrete sweeping mode with a maximum applied field of 1 T and an increment of 5 mT. Hysteresis parameters (M_s, M_{rs}, and B_c) were determined after high-field slope correction (> 700 mT) to remove diamagnetic and paramagnetic contributions. B_{cr} was obtained by progressively demagnetizing a saturated IRM in a reverse field down to −1 T. IRM acquisition curves were measured using logarithmically spaced field steps (120 steps, 10 μT-1T) and decomposed into cumulative log-Gaussian coercivity distributions following methods of refs. 69,70. FORC diagrams were acquired at maximum applied fields of 1 T and 1.02 mT increments, and processed with FORCinel software (version 3.08) with smoothing parameters Sc0 = 3, Sb0 = 4, and Sc1 = Sb1 = 7 (refs. 71,72).

3D XRM

Non-destructive three-dimensional imaging was performed using a ZEISS Xradia 610 Versa 3D XRM. Initial scanning of the full gelatin capsule containing the CE6 soils was conducted at a 4X objective lens at 60 kV tube voltage and 6.5 W power, achieving voxel resolution of ~1 μm. Imaging employed vertical stitching, capturing 3001 projections per tomography segment, each with a 3-second exposure. Higher-resolution imaging targeted specific regions of interest (ROIs) using a 20X objective lens at an 80 kV tube voltage and 10 W power, achieving voxel resolution of ~500 nm. Each ROI scan consisted of 3001 projections with 8-second exposure per projection 3D reconstructions and mineral segmentation were conducted using Object Research Systems (ORS) Dragonfly Pro software (v. 2024.1).

SEM and FIB-SEM

SEM and FIB-SEM analyses were conducted using a Zeiss CrossBeam 550 equipped with a Gemini II SEM column, a Capela Ga-liquid metal ion (Ga-LMIS) FIB column, and an Oxford Ultim Max EDXS detector. Prior to SEM imaging, samples were coated with a ~ 10 nm carbon layer to ensure conductivity; for FIB milling, target regions received an additional ~100 nm tungsten cap to minimize ion-beam damage. BSE-SEM images were acquired at accelerating voltages of 5–10 kV, while EDXS elemental distribution mapping utilized voltages of 5–15 kV. High-resolution BSE-SEM images (1 nm/pixel) were captured using Atlas 5 (v5.3) to document metallic Fe and Fe–Ni alloy distributions within agglutinates, glassy agglutinates, and volcanic glass matrices. Ultrathin (~ 100 nm) sections for TEM analysis were prepared by FIB milling at accelerating voltages of 3–15 kV and beam currents ranging from 30 nA (initial milling) to 100 pA (final polishing).

All datasets were processed in ORS Dragonfly Pro software (version 2024.1). Strong compositional contrast enabled initial segmentation via manual grayscale-thresholding of BSE-SEM images. Segmentation fidelity was verified visually and refined as needed. Particle morphometrics (major/minor axis lengths) were extracted using the "2D Aspect Ratio" module; coarse or irregular grains were measured via operator-assisted protocols to ensure robust statistics.

TEM

Conventional TEM analyses were performed using a JEOL JEM-2100 TEM instrument equipped with a LaB_6 electron gun, operating at 200 kV, and an Oxford X-Max EDXS detector. Atomic-scale high-resolution imaging and chemical analyses were conducted using a ThermoScientific Spectra 300 aberration-correction (S)TEM system operating at 300 kV. This instrument features a double-corrected monochromated TEM, a high brightness Schottky field emission gun (X-FEG) with a monochromator, a HAADF-STEM detector, and a Super-X EDXS detector, enabling atomic-level structural and compositional characterization.

Data availability

Source data are provided with this paper. All data generated in this study are provided in the Supplementary Information/Data file and deposited in the Figshare repository (https://doi.org/10.6084/m9.figshare.29411408.v2).

References

1. Fuller, M. & Cisowski, S. Lunar paleomagnetism. *Geomag* **2**, 307–455 (1987).
2. Blewett, D. T. et al. Lunar swirls: Examining crustal magnetic anomalies and space weathering trends. *J. Geophys. Res. Planets* **116**, E02002 (2011).
3. Weiss, B. P. & Tikoo, S. M. The lunar dynamo. *Science* **346**, 1246753 (2014).
4. Glotch, T. D. et al. Formation of lunar swirls by magnetic field standoff of the solar wind. *Nat. Commun.* **6**, 6189 (2015).
5. Wieczorek, M. A. et al. Lunar magnetism. *Rev. Mineral. Geochem.* **89**, 207–241 (2023).
6. Tikoo, S. M. et al. A two-billion-year history for the lunar dynamo. *Sci. Adv.* **3**, e1700207 (2017).
7. Cai, S. et al. A reinforced lunar dynamo recorded by Chang'e-6 farside basalt. *Nature* https://doi.org/10.1038/s41586-024-08526-2 (2024).
8. Cai, S. et al. Persistent but weak magnetic field at the Moon's midstage revealed by Chang'e-5 basalt. *Sci. Adv.* **11**, eadp3333 (2025).
9. Tarduno, J. A. et al. Absence of a long-lived lunar paleomagnetosphere. *Sci. Adv.* **7**, eabi7647 (2021).
10. Cottrell, R. D., Zhou, T. & Tarduno, J. A. Dataset of replicate Apollo sample magnetizations bearing on impacts and absence of a long-lived lunar dynamo. *Sci. Data* **11**, 807 (2024).
11. Wadhwa, M. Redox conditions on small bodies, the Moon and Mars. *Rev. Mineral. Geochem.* **68**, 493–510 (2008).
12. Zhang, H. et al. Long-term reduced lunar mantle revealed by Chang'e-5 basalt. *Nat. Commun.* **15**, 8328 (2024).
13. Rochette, P., Gattacceca, J., Ivanov, A. V., Nazarov, M. A. & Bezaeva, N. S. Magnetic properties of lunar materials: Meteorites, Luna and Apollo returned samples. *Earth Planet. Sci. Lett.* **292**, 383–391 (2010).
14. Sorokin, E. M. in *Advances in Geochemistry, Analytical Chemistry, and Planetary Sciences: 75th Anniversary of the Vernadsky Institute of the Russian Academy of Sciences* (eds Vladimir P. Kolotov & Natalia S. Bezaeva) 425-440 (Springer, Cham, 2023).
15. Heiken, G. H., Vaniman, D. T. & French, B. M. *Lunar Sourcebook, A User's Guide to the Moon*. (Cambridge, UK, 1991).
16. Rochette, P., Weiss, B. P. & Gattacceca, J. Magnetism of extraterrestrial materials. *Elements* **5**, 223–228 (2009).
17. Garrick-Bethell, I., Weiss, B. P., Shuster, D. L. & Buz, J. Early lunar magnetism. *Science* **323**, 356–359 (2009).
18. Mighani, S. et al. The end of the lunar dynamo. *Sci. Adv.* **6**, eaax0883 (2020).
19. Cisowski, S., Fuller, M., Rose, M. & Wasilewski, P. Magnetic effects of experimental shocking of lunar soil. *Geochim. Cosmochim. Acta* **4**, 3003 (1973).
20. Gattacceca, J. et al. Can the lunar crust be magnetized by shock: Experimental groundtruth. *Earth Planet. Sci. Lett.* **299**, 42–53 (2010).
21. Crawford, D. A. & Schultz, P. H. The production and evolution of impact-generated magnetic fields. *Int. J. Impact Eng.* **14**, 205–216 (1993).

22. Oran, R., Weiss, B. P., Shprits, Y., Miljković, K. & Tóth, G. Was the moon magnetized by impact plasmas?. *Sci. Adv.* **6**, eabb1475 (2020).
23. Garrick-Bethell, I. & Zuber, M. T. Elliptical structure of the lunar South Pole-Aitken basin. *Icarus* **204**, 399–408 (2009).
24. Hiesinger, H. et al. in *43rd Annual Lunar and Planetary Science Conference* 2863 (2012).
25. Evans, A. J. et al. Reexamination of early lunar chronology with GRAIL data: Terranes, basins, and impact fluxes. *J. Geophys. Res. Planets* **123**, 1596-1617 (2018).
26. Yue, Z. et al. Geological context of the Chang'e-6 landing area and implications for sample analysis. *Innovation* **5**, 100663 (2024).
27. Su, B. et al. South Pole–Aitken massive impact 4.25 billion years ago revealed by Chang'e-6 samples. *Natl. Sci. Rev.* nwaf103 (2025).
28. Wieczorek, M. A., Weiss, B. P. & Stewart, S. T. An impactor origin for lunar magnetic anomalies. *Science* **335**, 1212–1215 (2012).
29. Tsunakawa, H., Takahashi, F., Shimizu, H., Shibuya, H. & Matsushima, M. Surface vector mapping of magnetic anomalies over the Moon using Kaguya and Lunar Prospector observations. *J. Geophys. Res. Planets* **120**, 1160–1185 (2015).
30. Ivanov, M. A. et al. Geologic history of the northern portion of the South Pole-Aitken basin on the Moon. *J. Geophys. Res. Planets* **123**, 2585–2612 (2018).
31. Gou, S. et al. Complex basalt evolution in the Chang'e-6 landing area. *Earth Planet. Sci. Lett.* **648**, 119091 (2024).
32. Li, C. et al. Nature of the lunar far-side samples returned by the Chang'e-6 mission. *Natl. Sci. Rev.* **11**, nwae328 (2024).
33. Qian, Y. et al. First magnetic and spectroscopic constraints on attenuated space weathering at the Chang'e-5 landing site. *Icarus* **410**, 115892 (2024).
34. Cui, Z. et al. A sample of the Moon's far side retrieved by Chang'e-6 contains 2.83-billion-year-old basalt. *Science* **386**, 1395–1399 (2024).
35. Zhang, Q. W. L. et al. Lunar farside volcanism 2.8 billion years ago from Chang'e-6 basalts. *Nature*, https://doi.org/10.1038/s41586-024-08382-0 (2024).
36. Tauxe, L., Mullender, T. A. T. & Pick, T. Pothellies, wasp-waists, and superparamagnetism in magnetic hysteresis. *J. Geophys. Res.* **101**, 571–583 (1996).
37. Liu, Q. S. et al. Environmental magnetism: Principles and applications. *Rev. Geophys.* **50**, RG4002 (2012).
38. Roberts, A. P. et al. Resolving the origin of pseudo-single domain magnetic behavior. *J. Geophys. Res. Solid Earth* **122**, 9534–9558 (2017).
39. Morris, R. V. in *Lunar and Planetary Science Conference, 9th*. 2287-2297 (New York, Pergamon Press, 1978).
40. Morris, R. V. in *Lunar and Planetary Science C*onference, 11th. 1697-1712 (New York, Pergamon Press, 1980).
41. Muxworthy, A. & Williams, W. Critical single-domain grain sizes in elongated iron particles: Implications for meteoritic and lunar magnetism. *Geophys. J. Int.* **202**, 578–583 (2015).
42. Gaffney, A. M. et al. Magmatic evolution I: Initial differentiation of the Moon. *Rev. Mineral. Geochem.* **89**, 103–145 (2023).
43. Joy, K. H. et al. Lunar meteorites. *Rev. Mineral. Geochem*. **89**, 509–562 (2023).
44. Osinski, G. R. et al. Lunar impact features and processes. *Rev. Mineral. Geochem*. **89**, 339–371 (2023).
45. Gopon, P. et al. Metal impact and vaporization on the Moon's surface: Nano-geochemical insights into the source of lunar metals. *Meteorit. Planet. Sci.* **59**, 1775–1789 (2024).
46. Day, J. M. D. Metal grains in lunar rocks as indicators of igneous and impact processes. *Meteorit. Planet. Sci.* **55**, 1793–1807 (2020).
47. Colwell, J., Batiste, S., Horányi, M., Robertson, S. & Sture, S. Lunar surface: Dust dynamics and regolith mechanics. *Rev. Geophys* **45**, RG2006 (2007).
48. Citron, R., Smith, D., Stewart, S., Hood, L. & Zuber, M. The South Pole-Aitken basin: Constraints on impact excavation, melt, and ejecta. *Geophys. Res. Lett.* **51**, e2024GL110034 (2024).
49. Pasckert, J. H., Hiesinger, H. & van der Bogert, C. H. Lunar farside volcanism in and around the South Pole-Aitken basin. *Icarus* **299**, 538–562 (2018).
50. Qian, Y. et al. Long-lasting farside volcanism in the Apollo basin: Chang'e-6 landing site. *Earth Planet. Sci. Lett.* **637**, 118737 (2024).
51. Gu, L. et al. Space weathering of the Chang'e-5 lunar sample from a mid-high latitude region on the Moon. *Geophys. Res. Lett.* **49**, e2022GL097875 (2022).
52. Denevi, B. W. et al. Space weathering at the Moon. *Rev. Mineral. Geochem.* **89**, 611–650 (2023).
53. Xiong, M. et al. The formation mechanisms of np-Fe in lunar regolith: A review. *Mater* **17**, 5866 (2024).
54. Li, C. et al. Impact-induced ultra-high melting point oldhamite discovered in Chang'e-6 lunar soil. *Nat. Commun.* **16**, 2155 (2025).
55. Harrison, R. J. & Feinberg, J. M. Mineral magnetism: Providing new insights into geoscience processes. *Elements* **5**, 209–215 (2009).
56. Garrick-Bethell, I. & Weiss, B. P. Kamacite blocking temperatures and applications to lunar magnetism. *Earth Planet. Sci. Lett.* **294**, 1–7 (2010).
57. Górka-Kostrubiec, B. & Szczepaniak-Wnuk, I. Magnetic study of a mixture of magnetite and metallic iron in indoor dust samples. *Air Qual. Atmos. Hlth.* **10**, 105–116 (2017).
58. Devienne, J. A., Berndt, T. A., Williams, W. & Nagy, L. Magnetic recording stability of taenite-containing meteorites. *Geophys. Res. Lett.* **50**, e2022GL102602 (2023).
59. Devienne, J. A., Berndt, T. A., Williams, W. & Chen, S. From disorder to order: Inheritance of magnetic remanence in tetrataenite-bearing meteorites from multi-phase micromagnetic modeling. *J. Geophys. Res. Planets* **129**, e2023JE008268 (2024).
60. Shea, E. K. et al. A long-lived lunar core dynamo. *Science* **335**, 453–456 (2012).
61. Zhou, T. et al. A lunar core dynamo limited to the Moon's first ~140 million years. *Commun. Earth Environ.* **5**, 456 (2024).
62. Lawrence, K., Johnson, C., Tauxe, L. & Gee, J. Lunar paleointensity measurements: Implications for lunar magnetic evolution. *Phys. Earth Planet. Inter.* **168**, 71–87 (2008).
63. Nagy, L., Williams, W., Tauxe, L., Muxworthy, A. R. & Ferreira, I. Thermomagnetic recording fidelity of nanometer-sized iron and implications for planetary magnetism. *Proc. Natl. Acad. Sci.* **116**, 1984–1991 (2019).
64. Tikoo, S. M. & Evans, A. J. Dynamos in the inner Solar System. *Annu. Rev. Earth Planet. Sci.* **50**, 99–122 (2022).
65. Gattacceca, J. & Rochette, P. Toward a robust normalized magnetic paleointensity method applied to meteorites. *Earth Planet. Sci. Lett.* **227**, 377–393 (2004).
66. Yu, Y. Paleointensity determination using anhysteretic remanence and saturation isothermal remanence. *Geochem. Geophy. Geosy.* **11**, Q02Z12 (2010).
67. Fu, R. R., Lima, E. A., Volk, M. W. R. & Trubko, R. High-sensitivity moment magnetometry with the quantum diamond microscope. *Geochem. Geophy. Geosy.* **21**, e2020GC009147 (2020).
68. Buz, J. et al. Magnetism of a very young lunar glass. *J. Geophys. Res. Planets* **120**, 1720–1735 (2015).
69. Robertson, D. J. & France, D. E. Discrimination of remanence-carrying minerals in mixtures, using isothermal remanent magnetisation acquisition curves. *Phys. Earth Planet. Inter.* **82**, 223–234 (1994).
70. Kruiver, P. P., Dekkers, M. J. & Heslop, D. Quantification of magnetic coercivity components by the analysis of acquisition curves of isothermal remanent magnetisation. *Earth Planet. Sci. Lett.* **189**, 269–276 (2001).

71. Harrison, R. J. & Feinberg, J. M. FORCinel: An improved algorithm for calculating first-order reversal curve distributions using locally weighted regression smoothing. *Geochem. Geophy. Geosy.* **9**, Q05016 (2008).
72. Egli, R. VARIFORC: An optimized protocol for calculating non-regular first-order reversal curve (FORC) diagrams. *Glob. Planet. Change* **110**, 302–320 (2013).
73. Wieczorek, M. A. et al. The crust of the Moon as seen by GRAIL. *Science* **339**, 671–675 (2013).
74. Kring, D. A., Kallenborn, D. P. & Collins, G. S. Grand canyons on the Moon. *Nat. Commun.* **16**, 1146 (2025).

Acknowledgements

We sincerely thank the Chinese Chang'e Lunar Exploration Project staff for their dedicated efforts in returning lunar samples. The authors also acknowledge funding from the National Natural Science Foundation of China (Grant number 42225402) to JH.L., the National Natural Science Foundation of China (Grant number 42388101) to YX.P., the Innovation Group Project of Southern Marine Science and Engineering Guangdong Laboratory (Zhuhai) (Grant number 311021003) to JH.L. and the Key Research Program of the Institute of Geology & Geophysics, CAS (Grant number IGGCAS-202401, Grant number IGGCAS-202202) to JH.L. We gratefully acknowledge Mr. Jian Ding and Dr. Xuechao Sha for assistance with electron microscopy, and Dr. Weiyang, Dr. Hengci Tian, and Ms. Hongxia Ma for assistance with sample preparation.

Author contributions

JH.L. and YX.P. conceived and designed the study. JH.L., L.X., Y.L., KL.Z., WW.W., JW.L., YQ.W. and ZY.C. prepared the samples, conducted experiments, and analyzed data. JH.L. and Z.G. wrote the manuscript with substantial input from Y.L., KL.Z., L.X. and YX.P. X.T., LX.G., Y.C., QL.L., SH.C. and SC.L. participated in scientific discussions, reviewed, and edited the manuscript.

Competing interests

The authors declare no competing interests.

Additional information

Supplementary information The online version contains supplementary material available at https://doi.org/10.1038/s41467-025-61705-1.

Correspondence and requests for materials should be addressed to Jinhua Li.

Peer review information *Nature Communications* thanks Huapei Wang, Benjamin Weiss and the other, anonymous, reviewer(s) for their contribution to the peer review of this work. A peer review file is available.